CORA Cork Open Research Archive
Cartlann Taighde Oscailte Chorcaí

Title	Doping controlled roughness and defined mesoporosity in chemically etched silicon nanowires with tunable conductivity
Authors	McSweeney, William;Lotty, Olan;Mogili, N. V. V.;Glynn, Colm;Geaney, Hugh;Tanner, David A.;Holmes, Justin D.;O'Dwyer, Colm
Publication date	2013-07-18
Original Citation	McSweeney, W., Lotty, O., Mogili, N. V. V., Glynn, C., Geaney, H., Tanner, D., Holmes, J. D. and O'Dwyer, C. (2013) 'Doping controlled roughness and defined mesoporosity in chemically etched silicon nanowires with tunable conductivity', Journal of Applied Physics, 114(3), 034300 (11 pp). doi: 10.1063/1.4813867
Type of publication	Article (peer-reviewed)
Link to publisher's version	http://scitation.aip.org/content/aip/journal/jap/114/3/10.1063/1.4813867 - 10.1063/1.4813867
Rights	© 2013 AIP Publishing LLC
Download date	2026-11-15 16:43:41
Item downloaded from	https://hdl.handle.net/10468/2408

UCC
University College Cork, Ireland
Coláiste na hOllscoile Corcaigh

AIP | Journal of Applied Physics

Doping controlled roughness and defined mesoporosity in chemically etched silicon nanowires with tunable conductivity

W. McSweeney, O. Lotty, N. V. V. Mogili, C. Glynn, H. Geaney, D. Tanner, J. D. Holmes, and C. O'Dwyer

Citation: Journal of Applied Physics **114**, 034309 (2013); doi: 10.1063/1.4813867
View online: http://dx.doi.org/10.1063/1.4813867
View Table of Contents: http://scitation.aip.org/content/aip/journal/jap/114/3?ver=pdfcov
Published by the AIP Publishing

Articles you may be interested in

Investigation of direct current electrical properties of electrochemically etched mesoporous silicon carbide
J. Appl. Phys. **116**, 223705 (2014); 10.1063/1.4904085

Near-infrared emission from mesoporous crystalline germanium
AIP Advances **4**, 107128 (2014); 10.1063/1.4898643

The role of surface states in modification of carrier transport in silicon nanowires
J. Appl. Phys. **113**, 193703 (2013); 10.1063/1.4805031

The effects of size and orientation on magnetic properties and exchange bias in Co3O4 mesoporous nanowires
J. Appl. Phys. **109**, 07B520 (2011); 10.1063/1.3548831

Correlating dopant distributions and electrical properties of boron-doped silicon nanowires
Appl. Phys. Lett. **95**, 162101 (2009); 10.1063/1.3250431



Reuse of AIP Publishing content is subject to the terms at: https://publishing.aip.org/authors/rights-and-permissions. IP: 143.239.102.113 On: Fri, 19 Feb 2016 09:29:50

Doping controlled roughness and defined mesoporosity in chemically etched silicon nanowires with tunable conductivity

W. McSweeney,[1,2] O. Lotty,[3,4] N. V. V. Mogili,[5,6] C. Glynn,[1,3] H. Geaney,[1,3] D. Tanner,[5,6] J. D. Holmes,[1,3,4] and C. O'Dwyer[1,3,6,a)]
[1]*Department of Chemistry, University College Cork, Cork, Ireland*
[2]*Department of Physics and Energy, University of Limerick, Limerick, Ireland*
[3]*Micro & Nanoelectronics Centre, Tyndall National Institute, Lee Maltings, University College Cork, Cork, Ireland*
[4]*Centre for Research on Adaptive Nanostructures and Nanodevices (CRANN), Trinity College Dublin, Dublin 2, Ireland*
[5]*Department of Design & Manufacturing Technology, University of Limerick, Limerick, Ireland*
[6]*Materials & Surface Science Institute, University of Limerick, Limerick, Ireland*

(Received 6 March 2013; accepted 26 June 2013; published online 18 July 2013)

By using Si(100) with different dopant type (n^{++}-type (As) or p-type (B)), we show how metal-assisted chemically etched (MACE) nanowires (NWs) can form with rough outer surfaces around a solid NW core for p-type NWs, and a unique, defined mesoporous structure for highly doped n-type NWs. We used high resolution electron microscopy techniques to define the characteristic roughening and mesoporous structure within the NWs and how such structures can form due to a judicious choice of carrier concentration and dopant type. The n-type NWs have a mesoporosity that is defined by equidistant pores in all directions, and the inter-pore distance is correlated to the effective depletion region width at the reduction potential of the catalyst at the silicon surface in a HF electrolyte. Clumping in n-type MACE Si NWs is also shown to be characteristic of mesoporous NWs when etched as high density NW layers, due to low rigidity (high porosity). Electrical transport investigations show that the etched nanowires exhibit tunable conductance changes, where the largest resistance increase is found for highly mesoporous n-type Si NWs, in spite of their very high electronic carrier concentration. This understanding can be adapted to any low-dimensional semiconducting system capable of selective etching through electroless, and possibly electrochemical, means. The process points to a method of multiscale nanostructuring NWs, from surface roughening of NWs with controllable lengths to defined mesoporosity formation, and may be applicable to applications where high surface area, electrical connectivity, tunable surface structure, and internal porosity are required. © *2013 AIP Publishing LLC*.
[http://dx.doi.org/10.1063/1.4813867]

I. INTRODUCTION

The controlled formation of porosity and roughness in Si[1–3] still attracts substantial attention, and nanoscale Si in the form of nanocrystals,[4] nanowires (NWs), and mesoporous analogues have been successfully applied[5] to Li-ion batteries,[6] photovoltaics,[7] sensing,[8] and optoelectronics. Nanoscale Si in the form of NWs can be grown using bottom up approaches[9] in addition to top-down etching protocols, and have shown to be effective building blocks in nanoelectronic devices.[10] Porous semiconductor formation through electrochemical and chemical means, including silicon, are now very well known[5,11–15] and the fundamental basics of electrochemically and related methods for isotropic and crystallographically controlled etching have been established. The discovery of light-emitting nanoporous Si[3,16,17] propelled investigations of porosity formation in III−V[18–20] and other Group IV semiconductors[21,22] and II-VI materials.[23,24] The low cost and fabrication simplicity of etching routes allow Si to be fabricated with various structure-dependent properties useful in various applications in optical and photovoltaic materials[25,26] micro- and optoelectonics,[27,28] and chemical and biological sensors[8,29] due to its biocompatibility. For thermoelectric devices based on silicon,[30] the engineering of its structure to alter phonon dispersion via confinement, surface scattering and other processes is useful for controlling thermal conductivity.[31]

The ability to control the morphology and shape of silicon nanostructures by chemical etching in the presence of a redox couple in solution or using a metal/ion (metal-assisted chemical etching or MACE)[32–36] gives new routes toward complex silicon structures, where roughness and porosity within the nanostructures contribute to exploitable properties in device development. Many MACE methodologies[36] have been developed which can produce Si NWs with uniform diameters and packing densities.[35,37,38] Electrochemical etching can fine tune the direction and size of pore growth, which defined the remaining skeletal material. MACE,[40,41] however, can result in high sidewall roughness, and controlling this surface roughness and the transition to porosity[39] is a key challenge for reproducible large scale formation of functional nanoscale Si.

In energy storage applications, particularly as a possible alternative for Li-ion battery anodes, the low dimensionality

a)Email: c.odwyer@ucc.ie. Tel.: +353 21 490 2732. Fax: + 353 21 427 4097.

 © 2013 AIP Publishing LLC

Reuse of AIP Publishing content is subject to the terms at: https://publishing.aip.org/authors/rights-and-permissions. IP: 143.239.102.113 On: Fri, 19 Feb 2016 09:29:50

and porosity afforded by (electro)chemical etching is beneficial for accommodating volumetric expansion of the Si lattice during lithium insertion[40] and removal, and with electronic transport conceptually unaffected, an improvement in battery anode performance has been found using nanoscale Si.[6,41,42]

The doping type and density of the Si plays a major role in defining the type of etching,[15] and the resulting morphology for many of the parameters that affect the electrochemistry and etching of Si.[11,12] For n-type Si, porosity formation or nanostructure relief using potentiodynamic or potentiostatic methods, space-charge breakdown conditions must occur in the absence of light and the resulting nanoscale Si is often defined by the depletion layer width which in turn is set by the doping type and concentration. A key requirement for electroless etching methods is the need to define and control porosity formation. These methods of pore formation usually give a simple structure with uniform pore size through the pore opening to the pore bottom, because the pore size formed by these methods is often regulated by the silver (Ag) or gold (Au) used as catalyst.[43] Recent work has shown that the etching bath concentration is definitively linked to the degree of porosity within the wires, for a given doping type and concentration.[39,44] However, MACE does allow for large-scale, and rapid fabrication of high-quality,[45] well-aligned vertically oriented Si NWs with large area homogeneity and tunable depths, which for a given etching bath can be affected by substrate doping type and concentration. Previously reported studies show that some degree of porosity control is attained by tuning the Si resistivity (doping density), where a trend toward higher roughness with decreasing resistivity (or higher doping density)[4,46–48] is found. There are few formal investigations of the influence of doping concentration and doping type for both roughness and porosity formation[49] within NWs.

Here, we report a systematic investigation on the effect of doping type on the development of hierarchical roughness and defined mesoporosity in etched Si NWs using advanced microscopy and spectroscopy techniques. We show how the degree of etching can result in sub-5 nm labyrinthine features within n-type NWs resulting in a uniquely defined single crystal mesoporous Si NW (~2–3 nm pores). The mesoporosity exhibits a characteristic interfeature wavelength which defines a constant distance in all directions between the network of silicon nanocrystals that make up the mesoporous wire, independent of crystal orientation of the wafer or NW. This effect is shown to be related to characteristics of the doping density and depletion region width. Using convergent beam electron diffraction (CBED) and scanning transmission electron microscopy (STEM), we detail the type and degree of roughness that forms on their outer surfaces of p-type NWs through a balance between the redox potential of the oxidant and the doping (Fermi level) of the Si in a HF solution of known concentration and pH. Finally, we demonstrate that electrical conduction through the mesoporous n-type NWs that are depleted of charge carriers is significantly reduced compared roughened p-type NWs with solid cores.

II. EXPERIMENTAL

200 mm p-type B-doped Si(100) wafers (680 μm thickness) with a resistivity of 5–80 Ω cm, purchased from University Wafer, were used. n-type Si(100) wafers, As-doped with resistivity in the range of 0.001–0.005 Ω cm were also used under identical etching conditions. Substrates were immersed for a variety of times in a heated solution of 5%, 10%, or 12% HF containing varying amounts of $AgNO_3$ (0.02–0.10 mol dm^{-3}) and maintained at 50 °C using a thermostated water bath. After removing the substrates from the etching bath they were washed copiously with deionized water and then with concentrated nitric acid to remove unwanted Ag deposits. The length of the Si NWs was controlled by the etching time and etchant concentration, which was uniform across the entire substrate.

Scanning electron microscopy (SEM) of cleaved (011) cross-sections, (001) plan view and individual NWs were examined on a Hitachi S4800 FESEM operating at 5 kV and Energy dispersive X-ray (EDX) analysis was performed using a Hitachi SU70 equipped with an Oxford Instruments X-max 50 mm^2 solid-state EDX detector. TEM and CBED were conducted on a JEOL 2100F FEGTEM. The NWs were scraped onto holey carbon copper grids for analysis. For STEM/CBED analysis, a spot size of 1.5 nm was used, with a camera length of 40 cm using a condenser aperture of 100 μm. The CBED patterns were taken every 4.2 nm over a total analytical distance of 197.4 nm.

For metallization contacting to back sides of wafers, focused ion beam milling and TEM lamella preparation were conducted on a FEI 200 FIBSIMS workstation. A Pt capping layer was used for sample protection during lamella thinning to electron transparency. X-ray photoelectron spectroscopy (XPS) was acquired using a Kratos Axis 165 monochromatized X-ray photoelectron spectrometer equipped with a dual anode (Mg/Al) source. Survey spectra were captured at as pass energy (PE) of 100 eV, step size of 1 eV, and dwell time of 50 ms. The core level spectra were an average of 10 scans captured at a PE of 25 eV, step size of 0.05 eV, and dwell time of 100 ms. The spectra were corrected for charge shift to the C 1s line at a binding energy of 284.9 eV. A Shirley background correction was employed, and the peaks were fitted to Voigt profiles. X-ray diffraction (XRD) was conducted on a Philips X'pert MRDPro diffractometer using Cu Kα radiation.

Electrical contacting methodologies to develop low resistance ohmic contacts between the non-metallic substrates and the metal current collectors involved (a) *in situ* aluminium sputtering on Ar^+ plasma etched substrates (annealed and as-deposited), and (b) the formation of a Cu-In-Ga-Si sandwich after prior removal of the back SiO_2 layer. Current-voltage analysis was performed using a probe station and the potential controlled using a BIOLOGIC VSP.

III. RESULTS AND DISCUSSION

A. Morphology of p- and n-type Si NWs

Figure 1 shows the resulting Si NW layers that are formed using the (MACE) approach for low carrier density

Reuse of AIP Publishing content is subject to the terms at: https://publishing.aip.org/authors/rights-and-permissions. IP: 143.239.102.113 On: Fri, 19 Feb 2016 09:29:50

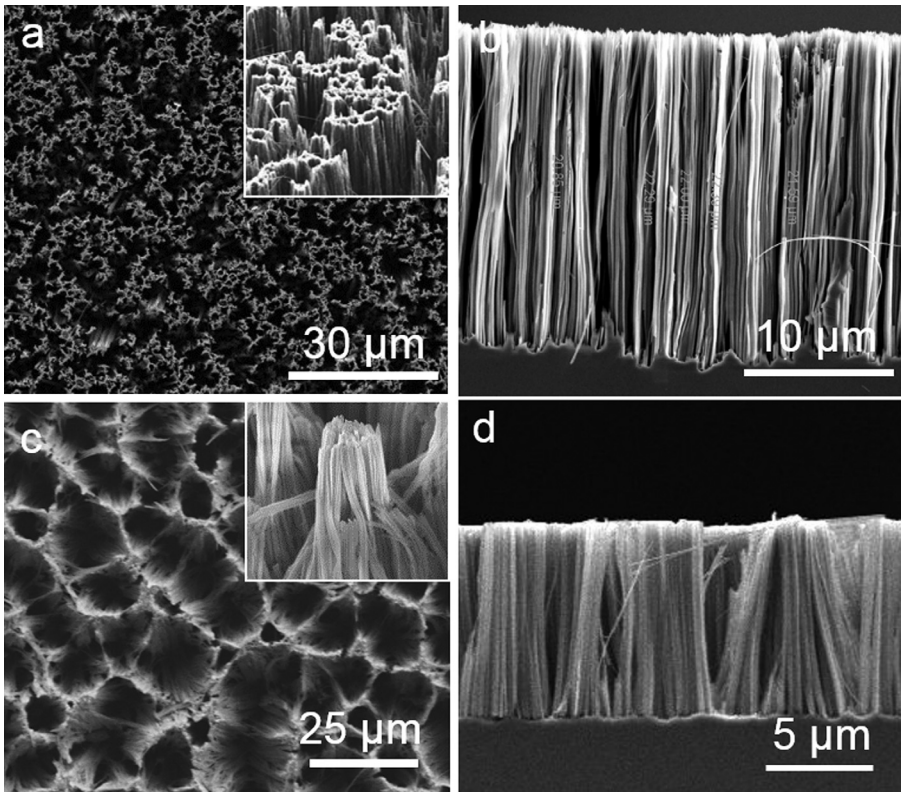


FIG. 1. (a) Plan view and (b) cross-sectional SEM images of p-type Si NWs etched in a HF solution containing 0.04 mol dm^{-3}. (c) Plan view and (d) cross-sectional SEM images of n-type Si NWs showing characteristic clumping after removal from the electrolyte.

p-type ($\sim 10^{15}\,cm^{-3}$) and highly doped n-type wafers ($\sim 10^{19}\,cm^{-3}$). Vertical arrays of NWs are formed across the entire surface of the wafer in the case of p-type NWs, as shown in the SEM images in Fig. 1. Figure 1(a) shows a random distribution of porosity in plan view, and Fig. 1(b) shows the majority of NWs maintain similar lengths for a given HF concentration and etching time. The n-type NWs in Figs. 1(c) and 1(d) characteristically clump even for NW lengths that are similar to p-type NWs. Examination of the top surface of the SiNW layers shows that the wires appear in non-uniform distributions characterized by clumped regions of high density NWs and correspondingly, regions of locally less density. Such clumping has been previously linked to capillary force effects, which for a given electrolyte, surface tension, and evaporation rate, is stronger for higher aspect ratio and long NWs within the layer. The NWs clump together at their tips, due to van der Waals or electrostatic charges on the newly formed surfaces, facilitated by capillary forces present during drying after liquid immersion.[50,51] A lower degree of surface etching compared to underlying porosity, however, would also cause a similar effect. Additionally, as detailed further on, the reduction of the Ag^{+} to Ag^{0} also has a spatial consideration since n-type NWs more readily reduce ionic Ag, allowing for a greater areal deposition of the metal per unit time on the surface of the Si. Inefficient removal of this Ag during nitric acid washing could contribute also to the reasons for surface clumping or pillaring of the NW dispersion.

Figure 1 shows that in both n-type and p-type NW layers, the NWs remain connected to the bulk substrate, which is important for electrical contacting and application of MACE NWs. Electrochemically, their use in sensing or in Li-ion batteries is aided by having NW electrically connected to their substrate by default, rather than through dispersion, so that the limitation in charging, sensing, or electrical-mediated property control can be reduced to the details specific to an individual NW.

SEM examination reveals that the NWs have lengths dictated by the etching duration. In Fig. 2(a), we show p-type NWs with an average and consistent length of $\sim 20\,\mu m$ in length and those etched to a length of $\sim 115\,\mu m$ (Fig. 2(b)), with a similar distribution as an effective porous Si layer. For n-type NWs, the length is also tunable through etching duration as shown in Fig. 2(c), where NWs can be controllably etched from $2\,\mu m$ to $75\,\mu m$. It was previously shown that length control was possible when the $AgNO_3$ concentration was varied between 0.02 and 0.06 mol dm^{-3}, above which the proportional increase in NW length ($\langle 100 \rangle$ etching depth) decreased.[39] Further examination shows that the less dense regions are not devoid of NWs, rather the NWs are bent towards each other forming the high density regions. It has been established that for an increase in porosity in Si (provided the geometry of the material does not drastically alter, i.e., aspect ratio, thickness, length, etc.,) its Young modulus can be reduced.[52] Therefore, any reduction in NW rigidity can lead to enhanced capillary coalescence[53] due to higher elasticity, allowing clumping to form when the conditions allow, i.e., during evaporative drying after extraction from solution. As will be detailed below, the p-type NWs maintain rigid Si cores, while n-type wires are highly mesoporous and thus less rigid, allowing them to clump together more readily than p-type wires even when considerably shorter in length. In addition, X-ray diffraction data[54] collected from both p-type and n-type NW layers, and from

Reuse of AIP Publishing content is subject to the terms at: https://publishing.aip.org/authors/rights-and-permissions. IP: 143.239.102.113 On: Fri, 19 Feb 2016 09:29:50

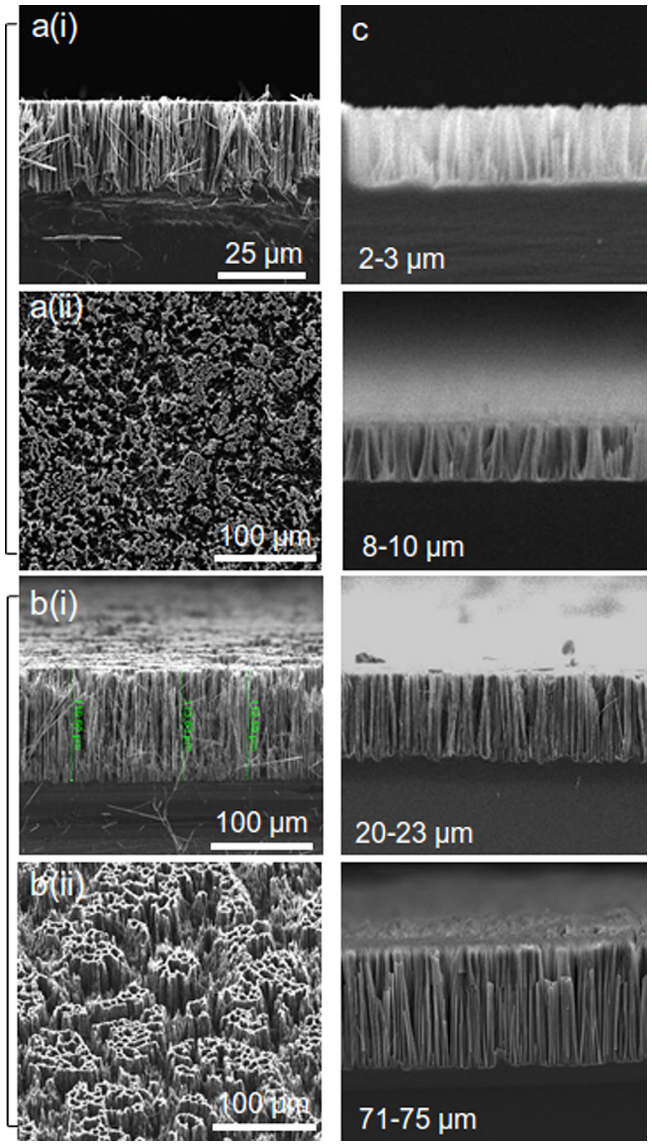


FIG. 2. (a-i) Cross-sectional and (a-ii) plan view SEM images of ~50 μm p-type NWs. (b) Cross-sectional and plan view SEM images of ~115 μm p-type NWs. (c) Cross-sectional SEM images of n-type Si NWs with lengths ranging from 2 to 75 μm. The typical range of NW lengths is indicated in each image.

corresponding Si(100) wafer coupons confirm phase purity after etching of both p-type and n-type NWs.

TEM analysis in Fig. 3 shows that the p-type NWs have a characteristic rough morphology but maintain a solid core, i.e., the non-planar outer surface is unevenly etched and no porosity forms within the NWs. The bright and two-beam dark field TEM images in Figs. 3(a) and 3(b) show that the surface roughness reveals facets of the Si crystal which appear as bright spots in the dark field images when viewed down a range of zone axes. The associated electron diffraction measurements in Fig. 3(c) also confirm their (100) orientation, consistent with etching from bulk Si(100), and that the uncontrollable deposition of Ag^+ oxidants preferentially etches the (100) facets leaving [100] oriented NWs. HRTEM analysis in Figs. 3(c) and 3(d) show the roughness of the surface which appears to be somewhat crystallographically defined, which confirms the electroless process of isotropic etching with different etch rates for each facet; fastest along $\langle 100 \rangle$, slowest along $\langle 111 \rangle$. The TEM examination also confirms the presence of a 2–3 nm native oxide and from the HRTEM image acquired along the (111) zone axis of the NW in Fig. 3(f), the entire wire including the roughened walls remains as a diamond cubic structure. Some degree of structural contortion can be caused by the presence of an oxide[4] due to tension caused at the interface with the silicon, particularly in regions of high aspect ratio roughness where the interfacial area between the rough features and the NW is of similar size to its distance away from that interface, and oxide formation can bend or twist such features.

The roughness of p-type NWs was also investigated by scanning and atomic resolution TEM allowing a surface roughness measurement without complications of features viewed in transmission. Simultaneously, convergent beam electron diffraction patterns were acquired and high order Laue zone (HOLZ) lines from the crystal lattice were monitored as a function of distance across the rough surface of a single NW in order to probe the crystallinity and relationship to the underlying bulk single crystal NW. In Figs. 4(a) and 4(b), the STEM images confirm that the nanoscale features on the rough NWs stem from non-uniform Si etching at the pore walls during electroless dissolution. No mesoporosity is found within p-type NWs at the carrier concentrations used. In order to assess the influence of roughness on the overall crystal phase of the NWs, 47 separate CBED patterns were acquired across the NW surface shown in Fig. 4(a). Each pattern was taken at a spatial position separated by 4.2 nm (spot diameter = 1 nm) across 197.4 nm of the NW surface.

Snap-shots from the analysis in Figs. 4(c)–4(e) show that the phase and strain sensitive HOLZ lines remained invariant across a surface that is nominally described as bevelled and rough. Effectively, the surface morphology roughening in p-type wires from the etching process predominantly retains its bulk crystallinity, and the roughness is due to removal of material, rather than a restructuring of the surface. Any misorientations of surface features would likely arise from oxidative strain or from a weak attachment to the NW wall in cases where locally more pronounced etching occurred.

Both p-type and n-type Si(100) substrates produce a dense array of nominally vertical NWs after etching. A statistically meaningful analysis of n-type NW diameter distributions was not possible due to clumping effects upon drying. However, from TEM analysis (see Sec. III C), the typical diameter, d, was found to be ~500 nm. For p-type wires, diameter distributions were measured from SEM images, and found to have a mean width of 80 nm as shown in Fig. 5(a) for NWs etched to nominal relief lengths of ~115 μm. This estimation accounts for neither roughness effects nor anisotropy in cross-sectional shape, although statistically, the variance is likely to be small. The roughness of the NWs was determined through image analysis of STEM data using a double tilt holder to image the surface morphology with a 5° off-axis tilt away from the [110] zone axis (Fig. 5(b)). A representative image is shown in Fig. 5(c), together with the average line profile from regions of the NW surface (Fig. 5(d)). The surface roughness was then determined using standard height-difference correlation

Reuse of AIP Publishing content is subject to the terms at: https://publishing.aip.org/authors/rights-and-permissions. IP: 143.239.102.113 On: Fri, 19 Feb 2016 09:29:50

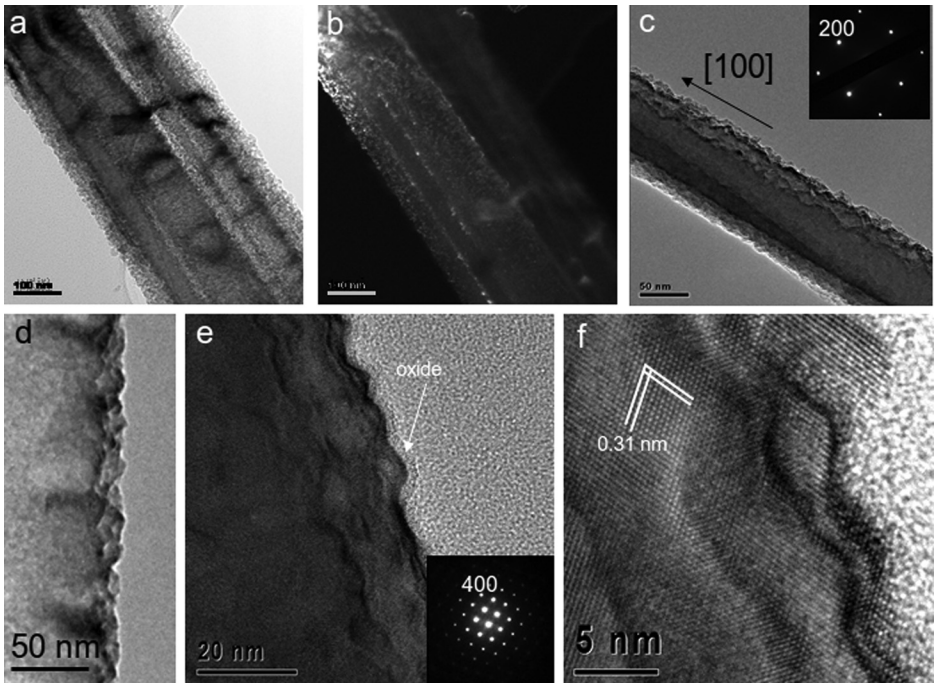


FIG. 3. TEM images of the MAC etched Si NWs showing the characteristic roughened outer surfaces. (a) Bright field and (b) high angle annular dark field TEM images of a single rough NW. The main core of the NW is not mesoporous. (c) A larger diameter NW showing roughened surfaces. The inset electron diffraction pattern confirms a diamond cubic structure with a (100) orientation. (d) Side profile of the roughness of a typical p-type NW. (e) and (f) HRTEM image of the NW outer surface showing characteristic roughness, oxide coating and the 0.31 nm {111} interplanar spacing characteristic of diamond cubic Si. The inset to (e) shows the [011] diffraction pattern.

function[55] $C(x) = \langle [z(x_0 + x) - \langle z \rangle][z(x_0) - \langle z \rangle] \rangle$, where $z(x_0)$ is the height at a point x_0, and x is the lateral separation between two surface points, can be written in terms of σ, ξ, and h as $C(x) = \sigma^2 \exp[-(|x|/\xi)^{2h}]$, where σ is the rms roughness given by $\sigma_{rms} = \left[\frac{1}{N}\sum_{n=1}^{N}(x_n^2)\right]^{1/2}$ and ξ the lateral correlation length given by the value of x at which the function decays to $1/e$. For the p-type Si NW, the morphology is dominated by a single length scale and so $h \approx 1$. In this approach, the amount of the diffuse component is determined by the rms roughness, and specifically, as x is much less than ξ, then $C(x) \propto \sigma^2$. The width of this component and its detailed shape give the lateral correlation length and the roughness parameter, respectively.

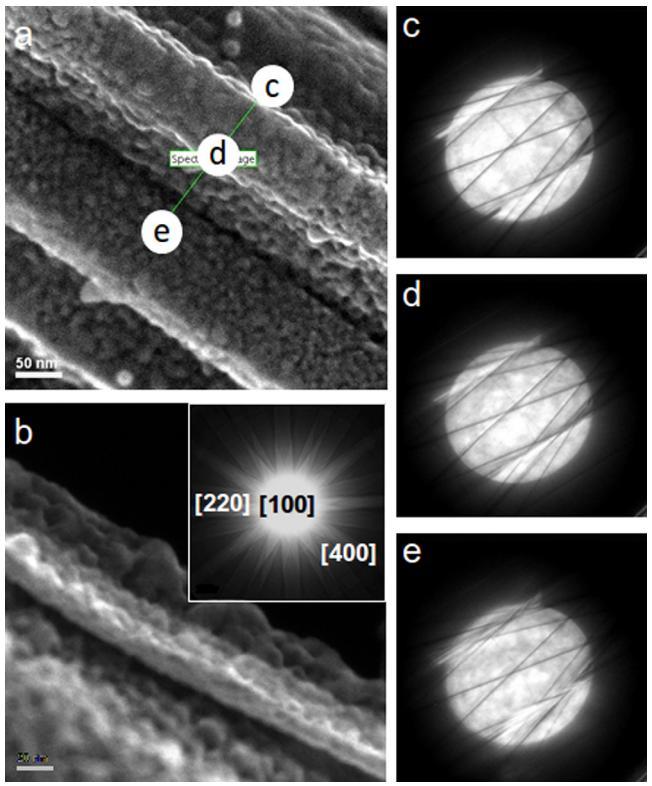


FIG. 4. (a) STEM image of a non-uniform NW rough surface. (b) HR-STEM image of the NW surface at a magnification of 1.2M× showing the nanoscale roughness features at the outer surface. (Inset) Kikuchi map acquired along the [011] zone axis of the overall NW confirming its (100) long axis orientation. (c)-(e) CBED patterns showing characteristics HOLZ lines taken from regions highlighted in (a) (enhanced online) [URL: http://dx.doi.org/10.1063/1.4813867.1].

Analysis of line profiles from STEM images of NWs, shown in Fig. 5(c) in the framework of the correlation gives typical values for rms roughness of 1.95 nm, with corresponding later correlation lengths of ~20–33 nm. NWs with such roughness are also known to have very effective phonon drag and softening effects which increase thermal resistance in thermoelectric based devices.[30]

The diameter of the NWs containing 2–3 nm of native oxide can now be refined to exclude a distance $\Delta d = 2\sqrt{2}\sigma$ arising from the rms roughness on each side of the NW. For the p-type NWs, this difference amounts to a reduction of 7%–10%. The method is general and applicable to very rough NWs where knowledge on the real diameter and its distribution is critical.

B. Compositional characterization of etched p-type Si NWs

The etching process is generally known to leave metallic Ag deposits, which are typically removed through a nitric acid-based wash. Owing to strong capillary forces which clump the NWs, the same effect is likely to prevent completely efficient removal of the reduced metallic Ag and also any reaction products from the electroless dissolution process that are not soluble in solution. Energy dispersive X-ray analysis and X-ray photoelectron spectroscopy of exfoliated Si NWs and Si NW layers were carried out to determine the

Reuse of AIP Publishing content is subject to the terms at: https://publishing.aip.org/authors/rights-and-permissions. IP: 143.239.102.113 On: Fri, 19 Feb 2016 09:29:50

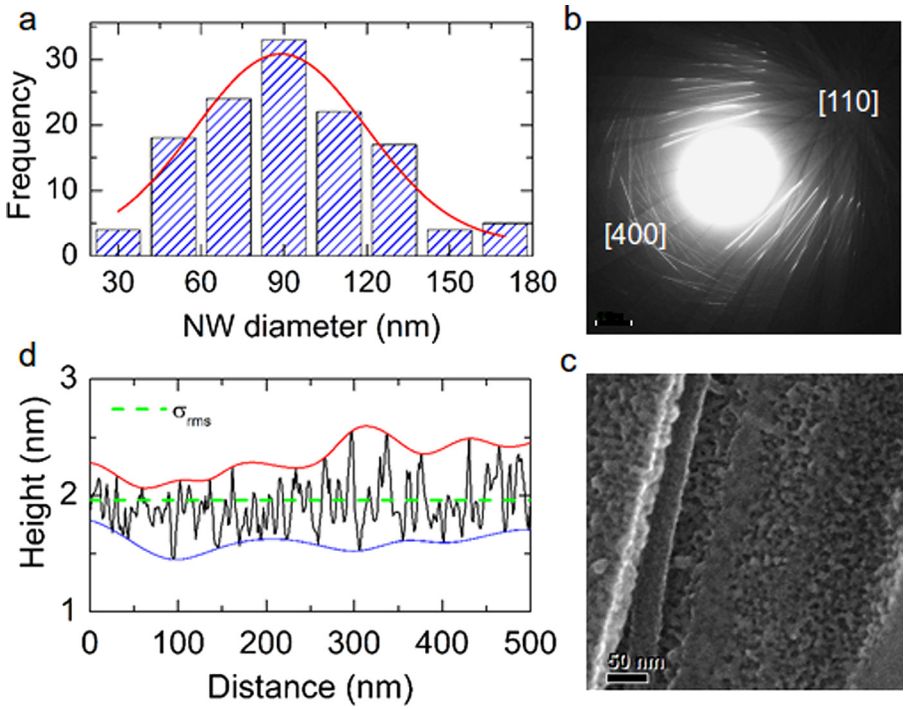


FIG. 5. (a) Histogram of the diameter distribution of 128 rough p-type NWs. (b) Kikuchi map corresponding to a 5° off-axis orientation of the NW along the [100] direction from the [110] axis. (c) STEM image of the rough NW surface. (d) Variation of roughness on the NW surface and the rms roughness of the measurements.

type of oxide formation on the NW surfaces and to quantify the local and global average concentrations of remnant impurities.

Figures 6(a)–6(c) show elemental maps of the Si and O Kα lines from several Si NWs. The Si NWs are predominantly coated with an oxide and it is uniformly distributed (in so far as can be determined taking variable roughness effects into account) along the entire length of the Si NW, consistent with HRTEM analysis in Fig. 2. Figure 6(e) shows the presence of metallic Ag on the surface of NWs after cleaning. The significant region of interest in Fig. 6(e) based on signal to noise ratio, are the central brighter regions which originates from Ag Kα radiation.[54] Dawood *et al.*[34] have reported some degree of surface enhanced resonance Raman scattering (SERRS) response for NWs after Ag-base MACE of Si and suggest that the ability of Ag to support a surface plasmon resonance[56] might be beneficial for sensing devices. Electrical field enhancement requires proximal Ag nanoparticles which requires a considerable density or remnant Ag to be in close proximity and unimpeded by the Si matrix in which it sits, or else larger structures with sharply defined edge that are close together, in order to provide an plasmonic enhancement of vibrational signal of adsorbed moieties on the NWs.[57]

Our EDX analysis suggests that the majority of the metallic Ag is removed and typically, only localized clumps remain, where found, rather than a distribution of metallic Ag at SERRS relative spatial densities within the roughened region of the surface. Clear signals from Ag^0 are characteristically found in areas with a larger density of wider diameter NWs indicating that the quantity and distribution are sufficiently small. The SERRS effect might be significant for Si NWs layers that are washed for a period of time that removes only the surface bound metallic dendrites that can typically form.[35] It is known that remnant nanoscale silver is lodged in the roughened pore walls of NWs to some extent. Related methods to introduce porosity relied on $AgNO_3$ concentrations an order of magnitude greater[46] than used in this work, resulting is a very high density of large Ag particle deposits. Re-oxidation in greater quantities of H_2O_2 does re-"activate"

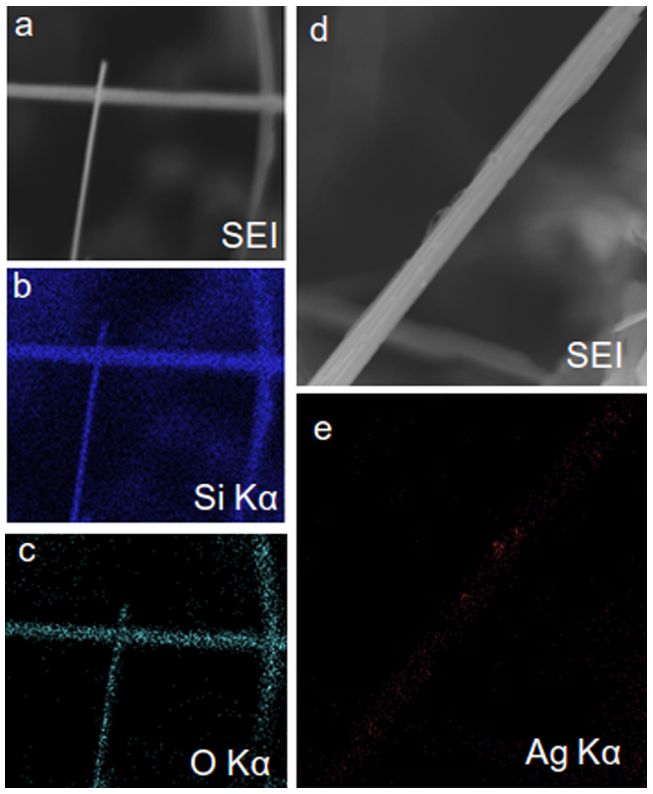


FIG. 6. (a)-(c) EDX mapping of the Si and O Kα X-ray lines showing oxide presence on the surface of NWs. (d) Secondary electron image and (e) EDX map of the Ag Kα line on a large NW.

Reuse of AIP Publishing content is subject to the terms at: https://publishing.aip.org/authors/rights-and-permissions. IP: 143.239.102.113 On: Fri, 19 Feb 2016 09:29:50

the process,[46] but effective removal of Ag is best with lower Ag^+ concentrations.

XPS spectra were also acquired for the rough p-type NW layers to quantitatively determine the metallic Ag content and to probe the stoichiometry of the surface oxide. In Fig. 7(a), the core-level spectra from the Si 2p core-levels are shown. Apart from the hyperfine Si 2p splitting, the presence of SiO_x and SiO_2 is confirmed from Si 2p and O 1s core-level spectra in Figs. 7(a) and 7(c). Specifically, the NW are predominantly coated with a stoichiometric SiO_2, identical to the bulk substrate, in spite of the roughened surface, which exposes many facets of the Si lattice to the Ag^+, allows for the dissolution of the Si. As will be outlined in Sec. III D, the maximum dissolution rate is limited by the conductivity and carrier type. For larger area investigations (greater density of NWs), the XPS spectra in Fig. 7(d) indicate the presence of very small quantities of remnant metallic Ag from the etching process. Quantitative measurements of the Ag content shows that the total concentration does not exceed 0.2%. As the porosity would nominally reduce any signal attenuation, this value is representative of the Ag content both on the surface and to a depth just below the rough features on the Si surface. Methods to control and form maximum possible, defined, mesoporosity by altering the substrate properties, rather than very high concentrations of Ag^+ is advantageous in biological applications, since Ag is strongly antimicrobial and difficult to remove in high aspect ratio porous structures.

C. Mesoporous n-type Si NWs

When n-type As-doped Si(100) with a carrier concentration of $\sim 10^{19}\,cm^{-3}$ underwent MACE with identical conditions to those of the p-type wires (etchant concentration and etching duration), we observed a marked transition to highly mesoporous morphology. A series of TEM images of the n-type NWs at various magnifications up to lattice resolution imaging of the silicon lattice, are shown in Fig. 8.

In Figs. 8(a) and 8(b), the TEM images show a labyrinthine structure that appears as a high density of white points consistent with pores when viewed in transmission. Through focal analysis of these regions confirms that they are voids within the material and high resolution imaging, shown in Fig. 8(c) confirms the random ordering of Si nanocrystallites interspersed with voids, characteristics of many mesoporous Si, silica,[58] Ge, and other semiconductors.[22,24] The morphology for electrochemically etched Si, or indeed MACE Si is unique and such a high mesopore density has not been previously observed. In Fig. 8(d), the mesoporous Si structure can be seen, comprising a network of nanoscale Si appearing as single crystallites but with interconnecting single crystal Si bridges. The structure of the Si is found to remain as diamond cubic and no observable defects (apart from the high surface area) are found in the crystal structure. For MACE NWs, one proposed mechanism[46] suggests that highly doped n-type NWs facilitate aggregation of large Ag particles and is reduced somewhat in the presence of a greater quantity of H_2O_2, which oxidizes Ag and reinitiates the etching condition. A trade-off must be considered in such cases between dissolved Ag, and the porosity and capillarity of the electrolyte within the NW layer so that effective and uniform redifussion of Ag^+ can be ascribed to an enhanced etching process. In our case, the dopant type as well as the concentration, formally define a controllable transition between a defined mesoporosity and roughening of a solid core NW, in a single step MACE process without H_2O_2, leaving the mesoporosity a function of the dopant type and concentration primarily. As will be shown below, these conditions (for a

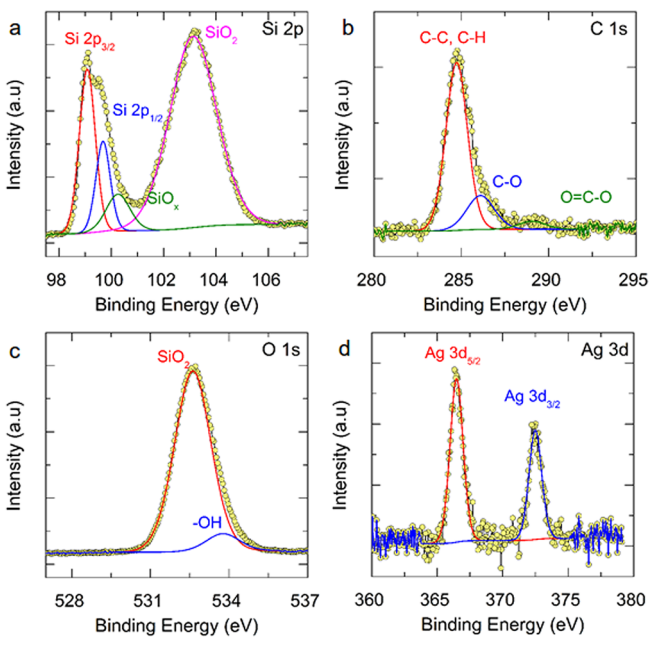


FIG. 7. XPS spectra from (a) Si 2p (b) C 1s, (c) O 1s, and (d) Ag 3d core-levels of p-type rough Si NW layers.

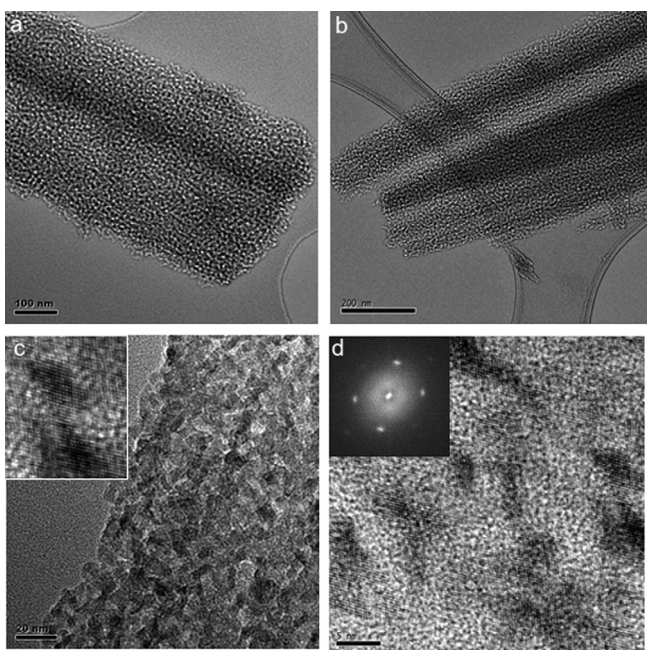


FIG. 8. TEM images of ((a), (b)) n-type Si NW and ((c), (d)) HRTEM images showing the random mesoporosity comprising nanoscale Si crystallites interspersed with voids. The FFT in (d) confirms two primary orientations of the 2D lattice resolved Si nanocrystal features.

Reuse of AIP Publishing content is subject to the terms at: https://publishing.aip.org/authors/rights-and-permissions. IP: 143.239.102.113 On: Fri, 19 Feb 2016 09:29:50

given Ag^+ and electrolyte concentration, ultimately define the maximum porosity and degree of etching within a NW.

The mesoporous nature of the n-type Si NWs is entirely different to the rough outer walls of the solid core p-type wires. The labyrinthine porosity is not ordered as found in mesoporous silicates or in ordered materials synthesized using bottom up approaches involving copolymer templates which are calcined out of the structure to leave pores, often in defined hexagonal or fcc geometries. Self-assembled or rationally grown mesoporosity typically forms ordered porosity. Here, the porosity is found on two length scales viz. the Si(100) wafer—porosification by formation of NWs in the bulk substrate and subsequent porosity formation within the NWs. The structure factors S(k), where k is the wave number associated with fast-Fourier-transform (FFT) of the arrangement of pores within the NWs and also the dispersion of the crystals comprising the skeletal Si, were determined by thresholding, and radially averaging the micrographs using image analysis. Figure 9(a) shows the thresholded image, while Fig. 9(b) shows the resulting intensity profile of the FFT, achieved by radial averaging of the FFT, yielding a dominant wavelength k, or distance between pores in all directions. The characteristic wavelength of the mesoporosity is obtained by $\lambda = 2\pi/k$, where k is the wave number corresponding to the maximum intensity of S(k) in Fig. 9.

The profile in Fig. 9(b) is a radially averaged plot of the FFT, and a distinct wavelength is observed. This distance (~12–15 nm) is the characteristic interpore distance in all direction through the n-type NW, despite of the distribution of mesopores being spatially random. The average pore sizes are in the range of 3–6 nm. However, as outlined in Sec. III E, this pore size and the interpore walls are formally dependent on the doping density and dopant type. Higher doping densities will result in narrow depletion layer widths, and will influence the maximum porosity attainable in case where internal porosity can form.

The schematic in Fig. 9(c) represents a possible scenario for ⟨100⟩ pore formation under conditions where the locality of the Ag^+ is random on the outer surface, and the etching mechanism proceeds with the accepted electroless etching via galvanic displacement. Where pores intersection from opposite sides of the NW, a variety of effective pore widths can be formed. Internal mesoporosity is thus formed by an availability of Ag^+ within the pores, allowing two further ⟨100⟩ directions to become available (up and down, for a laterally growing pore). All pores are formally separated by a distance similar to twice the depletion width, d_{sc} of the semiconductor (see Sec. III D). As the formation of internal pores is also random, the maximum density is possible when all locations are etched, with next-nearest neighbour pores separated by $2d_{sc}$. The tortuous and random nature of the mesoporosity is suggested to arise primarily from the random nature of Ag^+ deposition to initiate etching. Mass transport effects through pores within NWs will likely limit some pore formation, and deposition of metallic silver could potentially clog some pores. In many cases, pores can tunnel through the entirety of the NW leaving elliptical (where the major axis is twice the diameter of a pore) or circular (single) pores. This suggested arrangement of etching, merging,

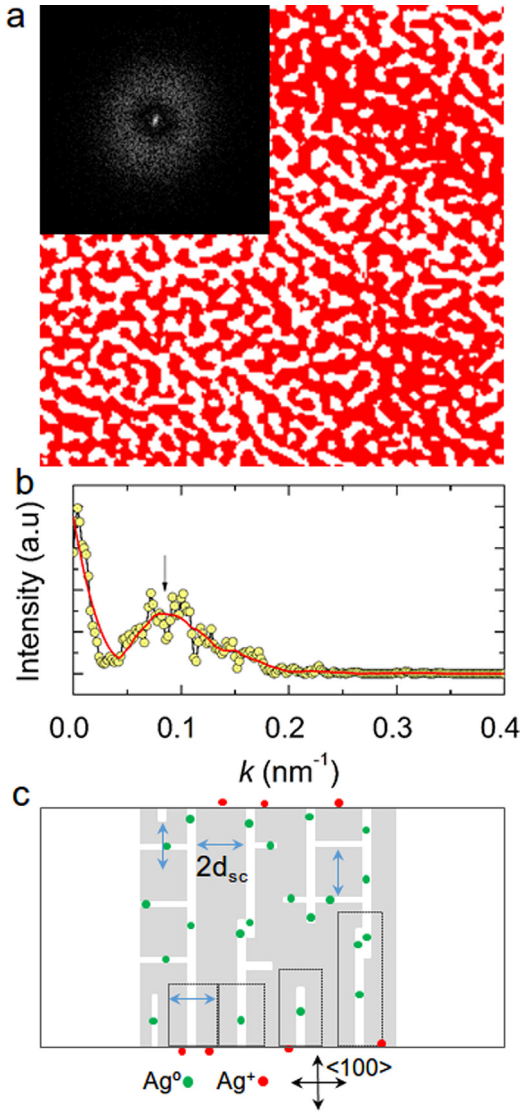


FIG. 9. Thresholded TEM image highlighting characteristic pore distributions. The inset shows the corresponding FFT and defined wavelength for the inter-pore distance within the mesoporous NW. (b) Radially averaged line profile of the FFT highlighting the characteristic wavelength k corresponding to the average interpore separation. (c) 2D schematic representation of ⟨100⟩ pore growth within a portion of a single NW leading to mesoporosity. Ag^+ on the surface of regions depleted of carriers is not reduced and no etching occurs.

overlapping and limited depth pores will occur in 3 dimensions throughout the NW, initiated by a random distribution of Ag^+ on the NW outer surface. The maximum porosity is achieved when every possible site on and in the pore is continually etched in 3D until all the remains is a carrier depleted skeleton of the silicon.

D. Etching mechanism and doping influence on rough versus mesoporous morphology

During the electroless etching of these wafers, the electrochemical potential for electron (e^-) injection/hole (h^+) consumption depends on the relative position of the Ag^+/Ag redox potential to that of the valence band of the semiconductor. Equally, hole injection and electron extraction are influenced by this redox potential in relation to the

Reuse of AIP Publishing content is subject to the terms at: https://publishing.aip.org/authors/rights-and-permissions. IP: 143.239.102.113 On: Fri, 19 Feb 2016 09:29:50

conduction band of an n-type semiconductor. Since the redox potential of Ag^+/Ag^0 lies below the valence band of Si,[59] lower p-type dopant concentrations (i.e., higher Fermi level energy) will cause the bands to bend less and decrease the depletion width at the NW surface; etching can proceed efficiently in the presence of the Ag^+ and continued etching at pore walls (NW surfaces) is possible due to non-uniform Ag^+ ion distribution on the surface and within pores, so long as the region in question is soaked in the electrolyte. In such cases, roughening of pore walls can occur.

The findings reported here concern the direct influence of the degree and type of doping, i.e., on the formation of solid core, rough-walled NWs, and mesoporous NWs with a defined intraporosity. We have previously confirmed the effect of $AgNO_3$ concentration change where we observed an increased porosity. This confirms that the quantity of Ag^+ is beneficial for a higher rate of etching since the energy barrier for interfacial charge transfer is reduced (59 mV/pH). Additionally, the fundamental band structure is more complex as the equilibrated Fermi level and redox potential of the Ag^+/Ag couple that changes with concentration,[60] locally accelerating the dissolution of the Si surface. This is also helped by a narrower depletion region for a given doping density,[37] because the etchant concentration has changed. In the absence of mass-transport limitations or material build up in narrow trenches of etched Si, the NW wall etching could continue due to the higher density of Ag^+ with time. The effect of doping and dopant type control is succinctly different to a rational increase in the concentration of $AgNO_3$ where porosity can sometimes be introduced into thinner wires, as well as by the mechanisms outlined above. The typical interpore distance between pores in the mesoporous n-type wires (~10 nm from Figs. 8 and 9) is similar to half of the depletion region[11] width $d_{n,p} \propto \sqrt{(2\varepsilon\varepsilon_0 V/qN_{D,A})}$, where V is the effective bias and $N_{D,A}$ is either the donor or acceptor density for n- or p-type Si, which is estimated to be ~17 nm based on the doping density of 10^{19} and a standard reduction potential (vs. standard hydrogen electrode (SHE)) of 2.04 V. Effectively, although not controlled by an applied potential, n-type NWs become mesoporous through continued etching of all possible Si facets in time, eventually stopping when the depletion region surrounding the skeletal Si within the NW overlaps; only limited further etching of the carrier depleted Si occurs, probably due to diffusion of h^+, known to occur in electrochemical pore growth phenomena.[18,19,61] This points to a method of multiscale nanostructuring NWs, from surface roughening to varying degrees with low doped p-type Si, and by exploiting the high doping density to define a mesoporous structure for n-type NWs. This hierarchical porosity control in the overall NW layer is predominantly controlled by interfacial charge transfer influenced by the Fermi level of the semiconductor, and the associated depletion region width.

For the n-type NWs, the mechanism allows a continued etching mechanism until depletion region overlap with the remaining skeletal mesoporous network causes carrier depletion. This effect plays a role in pore formation during potentiodynamic electrochemical dissolution of Si in HF electrolytes, but has not been observed for galvanic displacement or electroless etching reactions for Si NWs. Higher $AgNO_3$ concentrations, temperatures or etching time would be required for the p-type wires to becomes mesoporous, but increasing the p-type doping density would also increase the etch rate to allow a transition to mesoporous p-type wires, as was demonstrated by Balasundram *et al.*[49] In highly doped electrodes, h^+ diffusion would also be possible due to high carrier concentrations, allowing dissolution to occur away from the reduction site of the Ag at the interface with the Si. For the p-type and n-type Si used here, the h^+ diffusion lengths are at most on the order of 10^{-3} cm, and less for the lower h^+ mobility n-type Si.

E. Electrical conductivity of rough and mesoporous Si NWs

Because the NWs are inherently part of the original substrate from which they were etched, electrically contacting such anodes with a low resistance, ohmic contact, depends strongly on the conduction type and workfunction (φ_m) of the contact metal, and possibly from changes in conduction characteristics caused by the change in structure and increased disorder of an effectively porous NW surface.[62] Two-probe transport measurements through the NW layer-terminated wafers and the unetched wafers were acquired. Contacts were made by sputtering Al on the back of the Si NW electrodes *in situ* following Ar^+ plasma oxide removal. The contact were tested in sandwich geometries on bulk, unetched substrates to confidently test double-junction ohmicity variation due to porosification and size reduction of the Si on one side. In addition, an In-Ga eutectic was also employed so that electrical contact[63] could be made to a copper current collector. Figure 10 below shows the corresponding I-V curves for a series of metal contact sandwiches to unetched Si.

Figure 10(a) shows the characteristic I-V curves from 4 types of contacts: Cu/Si/Cu, Cu/Si/Cu annealed in air, Cu/Si/Cu annealed in vacuum, and a Cu/InGa/Si/InGa/Cu sandwich contact. The Cu-Si-Cu I-V exhibited a Schottky-like behavior with very low currents in the μA range, but with a significant Schottky barrier. Annealing this contact in air improved contact resistivity thus increasing current flow but retaining the unwanted rectifying response due to oxide formation on the Cu. The In-Ga eutectic on the other hand gives a good ohmic contact between the copper current collector and the Si anode, and is experimentally the quickest and simplest to form and replicate. Sputtered Al resulted in strongly rectifying behavior due to Al-Si intermetallic formation.[54] The ohmic contact gives a single-side contact resistance of ~33–36 Ω talking into account the ohmic drop across the 0.68 mm thick Si wafer with a resistivity of 5–80 Ω cm.

For p- and n-type Si NWs, comparison to bulk wafers was done using the In-Ga eutectic as an ohmic contact between the Si and copper current collector. Figure 10(b) shows that the mechanism of charge transport through the NWs is unaffected by the nanostructuring for both solid core, roughened p-type NWs which maintain a weak Schottky barrier, and highly mesoporous n-type NWs

Reuse of AIP Publishing content is subject to the terms at: https://publishing.aip.org/authors/rights-and-permissions. IP: 143.239.102.113 On: Fri, 19 Feb 2016 09:29:50

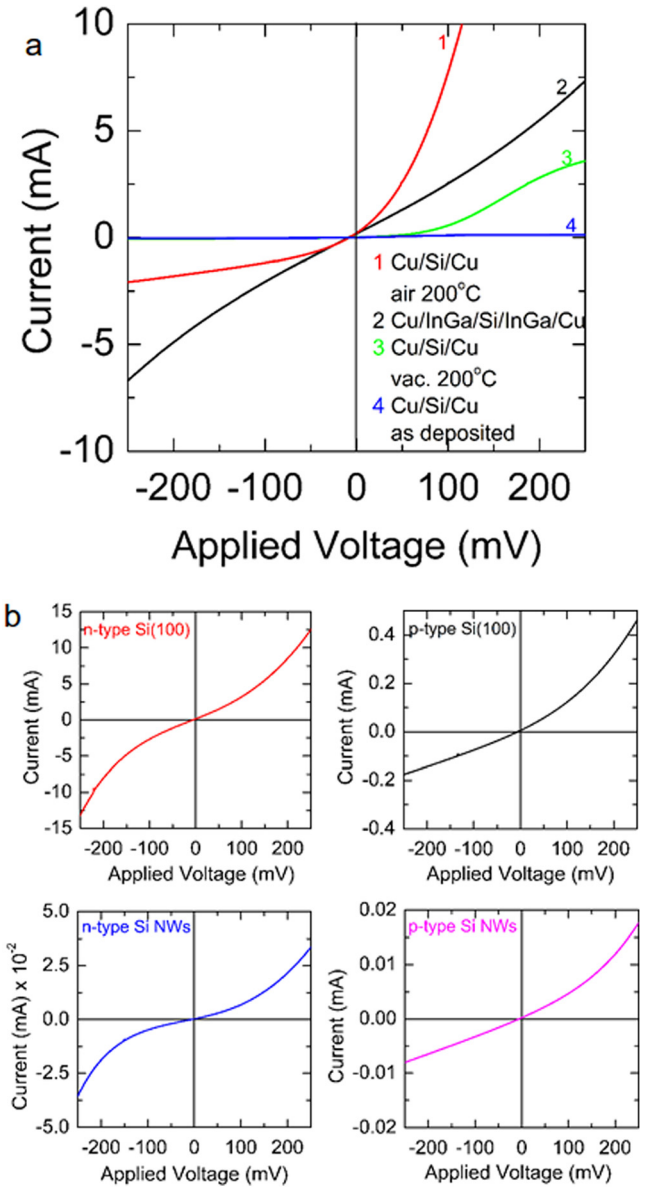


FIG. 10. (a) I-V curves from a series of Cu-contacted Si(100) electrodes. (b) I-V curves of Cu-contacted p-type and n-type Si NW electrodes.

maintain a thermionic emission based transport. For rough p-type NW, the differential conductivity in the higher bias regime is effectively reduced by a factor of ~20×, which includes contact resistance and resistance form interwire contacts within the layer. For n^{++}-type NWs however, the mesoporosity is shown to introduce significant resistance to charge transport, likely arising from the tortuous Si mesoporous network and the possibility for weakly linked Si bridges between all pores. Thus, in Fig. 10(b), we observe a reduction of ~300× in the high bias differential conductivity, in spite of a very high (10^{19} cm^{-3}) carrier concentration. This has important implications for Si NWs where porosity and electrical addressing are required, which is paramount for most electrically-driven device applications. While the conductivity decrease is not drastic, i.e., it does not approach a dielectric response and is still similar to medium doping density n-type silicon, the case of maximum mesoporosity does reduce effective conductivity. For thermoelectric applications, the Seebeck coefficient (S) and ZT will require a reduced thermal conductivity,[30] and improved S and ZT values will depend on an electrical conductivity reduction that is not greater than thermal resistance increase (compared to single crystal silicon wafers).

IV. CONCLUSIONS

Si NWs and unique mesoporous Si NWs have been fabricated by metal assisted chemical etching, where the NW length is controlled through etch process parameters. The roughening of the solid-core p-type NWs and the defined mesoporosity of n-type wires is possible without altering the material resistivity for a single dopant type, not by changing the catalyst metal. The etching process is controlled by the dopant type and the carrier density. The p-type NWs have a characteristic rough surface morphology while the n-type wires have a mesoporosity that is defined by equidistance pores in all directions, and the inter-pore distance is defined by the effective depletion region width at the reduction potential. This points to a method of multiscale nanostructuring NWs by exploiting the semiconductor-solution interface to influence surface roughening, and also to defined mesoporosity through single crystal NWs by altering dopant type and concentration. The remnant metallic Ag from the etch process is found to be very low (~0.2% concentration). In addition, the NWs are coated with a stoichiometric SiO_2. Clumping in n-type MACE Si NWs is also characteristic even for very short NWs due to low rigidity (high porosity). Electrical transport investigations show that low resistance, ohmic contacts to Cu current collectors can be achieved using an In-Ga eutectic, and that the highest resistance increase is found for highly mesoporous n-type Si NWs, in spite of their very high carrier concentration.

ACKNOWLEDGMENTS

W.M.S. acknowledges support under the framework of the INSPIRE programme, funded by the Irish Government's Programme for Research in Third Level Institutions, Cycle 4, National Development Plan 2007-2013. We also thank Dr Fathima Laffir for assistance with XPS measurements. The authors also acknowledge financial support from the European Union 7th Framework Programme under the SiNAPS project (Project Ref. No. 257856). C.G. acknowledges financial support from the Irish Research council under Award No. RS/2011/797. C.O.D. acknowledges support from Science Foundation Ireland under Award No. 07/SK/B1232a and from the UCC Strategic Research Fund.

[1]J. Wei, J. M. Buriak, and G. Siuzdak, Nature **399**, 243 (1999).
[2]V. Lehman and H. Föll, J. Electrochem. Soc. **137**, 653 (1990).
[3]L. T. Canham, Appl. Phys. Lett. **57**, 1046 (1990).
[4]A. I. Hochbaum, D. Gargas, Y. J. Hwang, and P. Yang, Nano Lett. **9**, 3550 (2009).
[5]J.-N. Chazalviel, *Porous Silicon Science and Technology* (Springer, Berlin, 1995).
[6]C. K. Chan, H. Peng, G. Liu, K. McIlwrath, X. F. Zhang, R. A. Huggins, and Y. Cui, Nat. Nanotechnol. **3**(1), 31 (2008).

Reuse of AIP Publishing content is subject to the terms at: https://publishing.aip.org/authors/rights-and-permissions. IP: 143.239.102.113 On: Fri, 19 Feb 2016 09:29:50

[7]T. Tsirlina, S. Cohen, H. Cohen, L. Spair, M. Peisach, R. Tenne, A. Matthaeus, S. Tiefenbacher, W. Jaegermann, E. A. Ponomarev, and C. Levy-Clement, Sol. Energy Mater. Sol. Cells **44**, 457 (1996).
[8]M. P. Stewart and J. M. Buriak, Adv. Mater. **12**, 859 (2000).
[9]J. D. Holmes, K. P. Johnston, R. C. Doty, and B. A. Korgel, Science **287**(5457), 1471–1473 (2000).
[10]Y. Cui and C. M. Lieber, Science **291**(5505), 851–853 (2001).
[11]R. L. Smith and S. D. Collins, J. Appl. Phys. **71**, R1 (1992).
[12]V. Lehman, *Electrochemistry of Silicon* (Wiley-VCH, Weinheim, Germany, 2002).
[13]K. W. Kolasinski, Curr. Opin. Solid State Mater. Sci. **9**, 73 (2005).
[14]A. Uhlir, Bell Syst. Tech. J. **35**, 333 (1956).
[15]M. I. J. Beale, J. D. Benjamin, M. J. Uren, N. G. Chew, and A. G. Cullis, J. Cryst. Growth **73**, 622 (1985).
[16]L. T. Canham, Properties of Porous Silicon (The Institution of Electrical Engineers, London, 1997).
[17]A. G. Cullis and L. T. Canham, Nature **353**, 335 (1991).
[18]C. O'Dwyer, D. N. Buckley, D. Sutton, and S. B. Newcomb, J. Electrochem. Soc. **153**, G1039 (2006).
[19]C. O'Dwyer, D. N. Buckley, D. Sutton, M. Serantoni, and S. B. Newcomb, J. Electrochem. Soc. **154**, H78 (2007).
[20]I. M. Tiginyanu, V. V. Ursaki, E. Monaico, E. Foca, and H. Föll, Electrochem. Solid-State Lett. **10**, D127 (2007).
[21]D. Sun, A. E. Riley, A. J. Cadby, E. K. Richman, S. D. Korlann, and S. H. Tolbert, Nature **441**, 1126 (2006).
[22]G. S. Armatas and M. G. Kanatzidis, Science **313**, 817 (2006).
[23]J. L. Mohanan, I. U. Arachchige, and S. L. Brock, Science **307**, 397 (2005).
[24]S. Bag, P. N. Trikalitis, P. J. Chupas, G. S. Armatas, and M. G. Kanatzidis, Science **317**, 490 (2007).
[25]X. Wen, L. V. Dao, and P. Hannaford, J. Phys. D: Appl. Phys. **40**, 3573 (2007).
[26]X. Li, Curr. Opin. Solid State Mater. Sci. **16**, 71 (2012).
[27]A. I. Hochbaum, R. Fan, R. R. He, and P. D. Yang, Nano Lett. **5**, 457 (2005).
[28]V. S.-Y. Lin, K. Motesharei, K.-P. S. Dancil, M. J. Sailor, and M. R. Ghadiri, Science **278**, 840 (1997).
[29]Y. Y. Li, F. Cunin, J. R. Link, T. Gao, R. E. Betts, S. H. Reiver, V. Chin, S. N. Bhatia, and M. J. Sailor, Science **299**(5615), 2045–2047 (2003).
[30]A. I. Hochbaum, R. K. Chen, R. D. Delgado, W. J. Liang, E. C. Garnett, M. Najarian, A. Majumdar, and P. D. Yang, Nature **451**, 163 (2008).
[31]J. P. Feser, J. S. Sadhu, B. P. Azeredo, K. H. Hsu, J. Ma, J. Kim, M. Seong, N. X. Fang, X. Li, P. M. Ferreira, S. Sinha, and D. G. Cahill, J. Appl. Phys. **112**, 114306 (2012).
[32]G. Oskam, J. G. Long, A. Natarajan, and P. C. Searson, J. Phys. D: Appl. Phys. **31**, 1927 (1998).
[33]S. Chattopadhyay, X. L. Li, and P. W. Bohn, J. Appl. Phys. **91**, 6134 (2002).
[34]M. K. Dawood, S. Tripathy, S. B. Dolmanan, T. H. Ng, H. Tan, and J. Lam, J. Appl. Phys. **112**, 073509 (2012).
[35]Y. Kato and S. Adachi, J. Electrochem. Soc. **158**, K157 (2011).
[36]A. I. Hochbaum and P. D. Yang, Chem. Rev. **110**, 527–546 (2010).
[37]K.-Q. Peng, Y.-J. Yan, S.-P. Gao, and J. Zhu, Adv. Mater. **14**, 1164 (2002).
[38]K. Q. Peng, J. J. Hu, Y. J. Yan, Y. Wu, H. Fang, Y. Xu, S. T. Lee, and J. Zhu, Adv. Funct. Mater. **16**, 387 (2006).
[39]O. Lotty, N. Petkov, Y. M. Georgiev, and J. D. Holmes, Jpn. J. Appl. Phys., Part 1 **51**, 11PE03 (2012).
[40]H. Wua and Y. Cui, Nano Today **7**, 414 (2012).
[41]A. Magasinki, P. Dixon, B. Hertzberg, A. Kvit, J. Ayala, and G. Yushin, Nature Mater. **9**, 353 (2010).
[42]M. Thakur, S. Sinsabaugh, M. J. Isaacson, M. S. Wong, and S. L. Biswal, Sci. Rep. **2**, 795 (2012).
[43]N. Geyer, B. Fuhrmann, Z. Huang, J. de Boor, H. S. Leipner, and P. Werner, J. Phys. Chem. C **116**, 13446 (2012).
[44]C. Chiappini, X. Liu, J. R. Fakhoury, and M. Ferrari, Adv. Funct. Mater. **20**, 2231 (2010).
[45]N. Geyer, Z. Huang, B. Fuhrmann, S. Grimm, M. Reiche, T.-K. Nguyen-Duc, J. d. Boor, H. S. Leipner, P. Werner, and U. Gosele, Nano Lett. **9**, 3106 (2009).
[46]X. Zhong, Y. Qu, Y.-C. Lin, L. Liao, and X. Duan, ACS Appl. Mater. Interfaces **3**, 261 (2011).
[47]M. G. Ghossoub, K. V. Valavala, M. Seong, B. Azeredo, K. Hsu, J. S. Sadhu, P. K. Singh, and S. Sinha, Nano Lett. **13**(4), 1564 (2013).
[48]J. Lim, K. Hippalgaonkar, S. C. Andrews, A. Majumdar, and P. Yang, Nano Lett. **12**(5), 2475 (2012).
[49]K. Balasundaram, J. S. Sadhu, J. C. Shin, B. Azeredo, D. Chanda, M. Malik, K. Hsu, J. A. Rogers, P. Ferreira, S. Sinha, and X. Li, Nanotechnology **23**, 305304 (2012).
[50]S.-W. Chang, V. P. Chuang, S. T. Boles, C. A. Ross, and C. V. Thompson, Adv. Funct. Mater. **19**, 2495 (2009).
[51]S. L. Cheng, C. H. Chung, and H. C. Lee, J. Electrochem. Soc. **155**, D711 (2008).
[52]H. Magoariec and A. Danescu, Phys. Status Solidi C **6**, 1680 (2009).
[53]J. Bico, B. Roman, L. Moulin, and A. Boudaoud, Nature **432**, 690 (2004).
[54]See supplementary material at http://dx.doi.org/10.1063/1.4813867 for X-ray diffraction analysis, EDX analysis, and I-V data.
[55]C. Diaz, M. L. Valenzuela, A. Laguna, V. Lavayen, J. Jimenez, L. A. Power, and C. O'Dwyer, Langmuir **26**, 10223–10233 (2010).
[56]W. Chern, K. Hsu, I. S. Chun, B. P. d. Azeredo, N. Ahmed, K. H. Kim, J. Zuo, N. Fang, P. Ferreira, and X. Li, Nano Lett. **10**, 1582 (2010).
[57]S.-Y. Chen, J. J. Mock, R. T. Hill, A. Chilkoti, D. R. Smith, and A. A. Lazarides, ACS Nano **4**, 6535 (2010).
[58]D. Zhao, Q. Huo, J. Feng, B. F. Chmelka, and G. D. Stucky, J. Am. Chem. Soc. **120**, 6024 (1998).
[59]P. Gorostiza, R. Diaz, J. Sevat, F. Sanz, and J. R. Morante, J. Electrochem. Soc. **144**, 909 (1997).
[60]C. M. Sanchez-Sanchez and A. J. Bard, Anal. Chem. **81**, 8094 (2009).
[61]R. P. Lynch, N. Quill, C. O'Dwyer, S. Nakahara, and D. N. Buckley, ECS Trans. **50**, 319 (2013).
[62]C. O'Dwyer, M. Szachowicz, G. Visimberga, V. Lavayen, S. B. Newcomb, and C. M. S. Torres, Nat. Nanotechnol. **4**, 239 (2009).
[63]O. V. Bilousov, J. J. Carvajal, D. Drouin, X. Mateos, F. Díaz, M. Aguiló, and C. O'Dwyer, ACS Appl. Mater. Interfaces **4**, 6927 (2012).

Reuse of AIP Publishing content is subject to the terms at: https://publishing.aip.org/authors/rights-and-permissions. IP: 143.239.102.113 On: Fri, 19 Feb 2016 09:29:50